

Measurement of Z^0 and Drell-Yan production cross sections using dimuons in $\bar{p}p$ collisions at $\sqrt{s}=1.8\text{ TeV}$

F. Abe,¹⁷ H. Akimoto,³⁹ A. Akopian,³¹ M. G. Albrow,⁷ A. Amadon,⁵ S. R. Amendolia,²⁷ D. Amidei,²⁰ J. Antos,³³ S. Aota,³⁷ G. Apollinari,³¹ T. Arisawa,³⁹ T. Asakawa,³⁷ W. Ashmanskas,¹⁸ M. Atac,⁷ P. Azzi-Bacchetta,²⁵ N. Bacchetta,²⁵ S. Bagdasarov,³¹ M. W. Bailey,²² P. de Barbaro,³⁰ A. Barbaro-Galtieri,¹⁸ V. E. Barnes,²⁹ B. A. Barnett,¹⁵ M. Barone,⁹ G. Bauer,¹⁹ T. Baumann,¹¹ F. Bedeschi,²⁷ S. Behrends,³ S. Belforte,²⁷ G. Bellettini,²⁷ J. Bellinger,⁴⁰ D. Benjamin,³⁵ J. Bensinger,³ A. Beretvas,⁷ J. P. Berge,⁷ J. Berryhill,⁵ S. Bertolucci,⁹ S. Bettelli,²⁷ B. Bevensee,²⁶ A. Bhatti,³¹ K. Biery,⁷ C. Bigongiari,²⁷ M. Binkley,⁷ D. Bisello,²⁵ R. E. Blair,¹ C. Blocker,³ K. Bloom,²⁰ S. Blusk,³⁰ A. Bodek,³⁰ W. Bokhari,²⁶ G. Bolla,²⁹ Y. Bonushkin,⁴ D. Bortoletto,²⁹ J. Boudreau,²⁸ L. Breccia,² C. Bromberg,²¹ N. Bruner,²² R. Brunetti,² E. Buckley-Geer,⁷ H. S. Budd,³⁰ K. Burkett,¹¹ G. Busetto,²⁵ A. Byon-Wagner,⁷ K. L. Byrum,¹ M. Campbell,²⁰ A. Caner,²⁷ W. Carithers,¹⁸ D. Carlsmith,⁴⁰ J. Cassada,³⁰ A. Castro,²⁵ D. Cauz,³⁶ A. Cerri,²⁷ P. S. Chang,³³ P. T. Chang,³³ H. Y. Chao,³³ J. Chapman,²⁰ M.-T. Cheng,³³ M. Chertok,³⁴ G. Chiarelli,²⁷ C. N. Chiou,³³ F. Chlebana,⁷ L. Christofek,¹³ R. Cropp,¹⁴ M. L. Chu,³³ S. Cihangir,⁷ A. G. Clark,¹⁰ M. Cobal,²⁷ E. Cocca,²⁷ M. Contreras,⁵ J. Conway,³² J. Cooper,⁷ M. Cordelli,⁹ D. Costanzo,²⁷ C. Couyoumtzelis,¹⁰ D. Cronin-Hennessy,⁶ R. Culbertson,⁵ D. Dagenhart,³⁸ T. Daniels,¹⁹ F. DeJongh,⁷ S. Dell'Agnello,⁹ M. Dell'Orso,²⁷ R. Demina,⁷ L. Demortier,³¹ M. Deninno,² P. F. Derwent,⁷ T. Devlin,³² J. R. Dittmann,⁶ S. Donati,²⁷ J. Done,³⁴ T. Dorigo,²⁵ N. Eddy,¹³ K. Einsweiler,¹⁸ J. E. Elias,⁷ R. Ely,¹⁸ E. Engels, Jr.,²⁸ W. Erdmann,⁷ D. Errede,¹³ S. Errede,¹³ Q. Fan,³⁰ R. G. Feild,⁴¹ Z. Feng,¹⁵ C. Ferretti,²⁷ I. Fiori,² B. Flaughner,⁷ G. W. Foster,⁷ M. Franklin,¹¹ J. Freeman,⁷ J. Friedman,¹⁹ H. Frisch,⁵ Y. Fukui,¹⁷ S. Gadomski,¹⁴ S. Galeotti,²⁷ M. Gallinaro,²⁶ O. Ganel,³⁵ M. Garcia-Sciveres,¹⁸ A. F. Garfinkel,²⁹ C. Gay,⁴¹ S. Geer,⁷ D. W. Gerdes,²⁰ P. Giannetti,²⁷ N. Giokaris,³¹ P. Giromini,⁹ G. Giusti,²⁷ M. Gold,²² A. Gordon,¹¹ A. T. Goshaw,⁶ Y. Gotra,²⁸ K. Goulianos,³¹ H. Grassmann,³⁶ L. Groer,³² C. Grosso-Pilcher,⁵ G. Guillian,²⁰ J. Guimaraes da Costa,¹⁵ R. S. Guo,³³ C. Haber,¹⁸ E. Hafen,¹⁹ S. R. Hahn,⁷ R. Hamilton,¹¹ T. Handa,¹² R. Handler,⁴⁰ W. Hao,³⁵ F. Happacher,⁹ K. Hara,³⁷ A. D. Hardman,²⁹ R. M. Harris,⁷ F. Hartmann,¹⁶ J. Hauser,⁴ E. Hayashi,³⁷ J. Heinrich,²⁶ A. Heiss,¹⁶ B. Hinrichsen,¹⁴ K. D. Hoffman,²⁹ M. Hohlmann,⁵ C. Holck,²⁶ R. Hollebeek,²⁶ L. Holloway,¹³ Z. Huang,²⁰ B. T. Huffman,²⁸ R. Hughes,²³ J. Huston,²¹ J. Huth,¹¹ H. Ikeda,³⁷ M. Incagli,²⁷ J. Incandela,⁷ G. Introzzi,²⁷ J. Iwai,³⁹ Y. Iwata,¹² E. James,²⁰ H. Jensen,⁷ U. Joshi,⁷ E. Kajfasz,²⁵ H. Kambara,¹⁰ T. Kamon,³⁴ T. Kaneko,³⁷ K. Karr,³⁸ H. Kasha,⁴¹ Y. Kato,²⁴ T. A. Keaffaber,²⁹ K. Kelley,¹⁹ R. D. Kennedy,⁷ R. Kephart,⁷ D. Kestenbaum,¹¹ D. Khazins,⁶ T. Kikuchi,³⁷ B. J. Kim,²⁷ H. S. Kim,¹⁴ S. H. Kim,³⁷ Y. K. Kim,¹⁸ L. Kirsch,³ S. Klimentenko,⁸ D. Knoblauch,¹⁶ P. Koehn,²³ A. Koenigter,¹⁶ K. Kondo,³⁷ J. Konigsberg,⁸ K. Kordas,¹⁴ A. Korytov,⁸ E. Kovacs,¹ W. Kowald,⁶ J. Kroll,²⁶ M. Kruse,³⁰ S. E. Kuhlmann,¹ E. Kuns,³² K. Kurino,¹² T. Kuwabara,³⁷ A. T. Laasanen,²⁹ S. Lami,²⁷ S. Lammel,⁷ J. I. Lamoureux,³ M. Lancaster,¹⁸ M. Lanzoni,²⁷ G. Latino,²⁷ T. LeCompte,¹ S. Leone,²⁷ J. D. Lewis,⁷ M. Lindgren,⁴ T. M. Liss,¹³ J. B. Liu,³⁰ Y. C. Liu,³³ N. Lockyer,²⁶ O. Long,²⁶ M. Loreti,²⁵ D. Lucchesi,²⁷ P. Lukens,⁷ S. Lusin,⁴⁰ J. Lys,¹⁸ K. Maeshima,⁷ P. Maksimovic,¹¹ M. Mangano,²⁷ M. Mariotti,²⁵ J. P. Marriner,⁷ G. Martignon,²⁵ A. Martin,⁴¹ J. A. J. Matthews,²² P. Mazzanti,² K. McFarland,³⁰ P. McIntyre,³⁴ P. Melese,³¹ M. Menguzzato,²⁵ A. Menzione,²⁷ E. Meschi,²⁷ S. Metzler,²⁶ C. Miao,²⁰ T. Miao,⁷ G. Michail,¹¹ R. Miller,²¹ H. Minato,³⁷ S. Miscetti,⁹ M. Mishina,¹⁷ S. Miyashita,³⁷ N. Moggi,²⁷ E. Moore,²² Y. Morita,¹⁷ A. Mukherjee,⁷ T. Muller,¹⁶ P. Murat,²⁷ S. Murgia,²¹ M. Musy,³⁶ H. Nakada,³⁷ T. Nakaya,⁵ I. Nakano,¹² C. Nelson,⁷ D. Neuberger,¹⁶ C. Newman-Holmes,⁷ C.-Y. P. Ngan,¹⁹ L. Nodulman,¹ A. Nomerotski,⁸ S. H. Oh,⁶ T. Ohmoto,¹² T. Ohsugi,¹² R. Oishi,³⁷ M. Okabe,³⁷ T. Okusawa,²⁴ J. Olsen,⁴⁰ C. Pagliarone,²⁷ R. Paoletti,²⁷ V. Papadimitriou,³⁵ S. P. Pappas,⁴¹ N. Parashar,²⁷ A. Parri,⁹ J. Patrick,⁷ G. Pauletta,³⁶ M. Paulini,¹⁸ A. Perazzo,²⁷ L. Pescara,²⁵ M. D. Peters,¹⁸ T. J. Phillips,⁶ G. Piacentino,²⁷ M. Pillai,³⁰ K. T. Pitts,⁷ R. Plunkett,⁷ A. Pompos,²⁹ L. Pondrom,⁴⁰ J. Proudfoot,¹ F. Ptohos,¹¹ G. Punzi,²⁷ K. Ragan,¹⁴ D. Reher,¹⁸ M. Reischl,¹⁶ A. Ribon,²⁵ F. Rimondi,² L. Ristori,²⁷ W. J. Robertson,⁶ A. Robinson,¹⁴ T. Rodrigo,²⁷ S. Rolli,³⁸ L. Rosenson,¹⁹ R. Roser,¹³ T. Saab,¹⁴ W. K. Sakumoto,³⁰ D. Saltzberg,⁴ A. Sansoni,⁹ L. Santi,³⁶ H. Sato,³⁷ P. Schlabach,⁷ E. E. Schmidt,⁷ M. P. Schmidt,⁴¹ A. Scott,⁴ A. Scribano,²⁷ S. Segler,⁷ S. Seidel,²² Y. Seiya,³⁷ F. Semeria,² T. Shah,¹⁹ M. D. Shapiro,¹⁸ N. M. Shaw,²⁹ P. F. Shepard,²⁸ T. Shibayama,³⁷ M. Shimojima,³⁷ M. Shochet,⁵ J. Siegrist,¹⁸ A. Sill,³⁵ P. Sinervo,¹⁴ P. Singh,¹³ K. Sliwa,³⁸ C. Smith,¹⁵ F. D. Snider,¹⁵ J. Spalding,⁷ T. Speer,¹⁰ P. Sphicas,¹⁹ F. Spinella,²⁷ M. Spiropulu,¹¹ L. Spiegel,⁷ L. Stanco,²⁵ J. Steele,⁴⁰ A. Stefanini,²⁷ R. Ströhmer,⁷ J. Strogilas,¹³ F. Strumia,¹⁰ D. Stuart,⁷ K. Sumorok,¹⁹ J. Suzuki,³⁷ T. Suzuki,³⁷ T. Takahashi,²⁴ T. Takano,²⁴ R. Takashima,¹² K. Takikawa,³⁷ M. Tanaka,³⁷ B. Tannenbaum,⁴ F. Tartarelli,²⁷ W. Taylor,¹⁴ M. Tecchio,²⁰ P. K. Teng,³³ Y. Teramoto,²⁴ K. Terashi,³⁷ S. Tether,¹⁹ D. Theriot,⁷ T. L. Thomas,²² R. Thurman-Keup,¹ M. Timko,³⁸ P. Tipton,³⁰ A. Titov,³¹ S. Tkaczyk,⁷ D. Tobeck,⁵ K. Tollefson,³⁰ A. Tollestrup,⁷ H. Toyoda,²⁴ W. Trischuk,¹⁴ J. F. de Troconiz,¹¹ S. Truitt,²⁰ J. Tseng,¹⁹ N. Turini,²⁷ T. Uchida,³⁷ F. Ukegawa,²⁶ J. Valls,³² S. C. van den Brink,¹⁵ S. Vejcek III,²⁰ G. Velev,²⁷ R. Vidal,⁷ R. Vilar,⁷ D. Vucinic,¹⁹ R. G. Wagner,¹ R. L. Wagner,⁷ J. Wahl,⁵ N. B. Wallace,²⁷ A. M. Walsh,³² C. Wang,⁶ C. H. Wang,³³ M. J. Wang,³³ A. Warburton,¹⁴ T. Watanabe,³⁷ T. Watts,³² R. Webb,³⁴ C. Wei,⁶ H. Wenzel,¹⁶ W. C. Wester III,⁷ A. B. Wicklund,¹ E. Wicklund,⁷ R. Wilkinson,²⁶ H. H. Williams,²⁶ P. Wilson,⁷ B. L. Winer,²³ D. Winn,²⁰ D. Wolinski,²⁰ J. Wolinski,²¹ S. Worm,²² X. Wu,¹⁰ J. Wyss,²⁷ A. Yagil,⁷ W. Yao,¹⁸ K. Yasuoka,³⁷ G. P. Yeh,⁷ P. Yeh,³³ J. Yoh,⁷ C. Yosef,²¹ T. Yoshida,²⁴ I. Yu,⁷ A. Zanetti,³⁶ F. Zetti,²⁷ and S. Zucchelli²

(CDF Collaboration)

- ¹Argonne National Laboratory, Argonne, Illinois 60439
²Istituto Nazionale di Fisica Nucleare, University of Bologna, I-40127 Bologna, Italy
³Brandeis University, Waltham, Massachusetts 02254
⁴University of California at Los Angeles, Los Angeles, California 90024
⁵University of Chicago, Chicago, Illinois 60637
⁶Duke University, Durham, North Carolina 27708
⁷Fermi National Accelerator Laboratory, Batavia, Illinois 60510
⁸University of Florida, Gainesville, Florida 32611
⁹Laboratori Nazionali di Frascati, Istituto Nazionale di Fisica Nucleare, I-00044 Frascati, Italy
¹⁰University of Geneva, CH-1211 Geneva 4, Switzerland
¹¹Harvard University, Cambridge, Massachusetts 02138
¹²Hiroshima University, Higashi-Hiroshima 724, Japan
¹³University of Illinois, Urbana, Illinois 61801
¹⁴Institute of Particle Physics, McGill University, Montreal, Canada H3A 2T8
and University of Toronto, Toronto, Canada M5S 1A7
¹⁵The Johns Hopkins University, Baltimore, Maryland 21218
¹⁶Institut für Experimentelle Kernphysik, Universität Karlsruhe, D-76128 Karlsruhe, Germany
¹⁷National Laboratory for High Energy Physics (KEK), Tsukuba, Ibaraki 305, Japan
¹⁸Ernest Orlando Lawrence Berkeley National Laboratory, Berkeley, California 94720
¹⁹Massachusetts Institute of Technology, Cambridge, Massachusetts 02139
²⁰University of Michigan, Ann Arbor, Michigan 48109
²¹Michigan State University, East Lansing, Michigan 48824
²²University of New Mexico, Albuquerque, New Mexico 87131
²³The Ohio State University, Columbus, Ohio 43210
²⁴Osaka City University, Osaka 588, Japan
²⁵Universita di Padova, Istituto Nazionale di Fisica Nucleare, Sezione di Padova, I-35131 Padova, Italy
²⁶University of Pennsylvania, Philadelphia, Pennsylvania 19104
²⁷Istituto Nazionale di Fisica Nucleare, University and Scuola Normale Superiore of Pisa, I-56100 Pisa, Italy
²⁸University of Pittsburgh, Pittsburgh, Pennsylvania 15260
²⁹Purdue University, West Lafayette, Indiana 47907
³⁰University of Rochester, Rochester, New York 14627
³¹Rockefeller University, New York, New York 10021
³²Rutgers University, Piscataway, New Jersey 08855
³³Academia Sinica, Taipei, Taiwan 11530, Republic of China
³⁴Texas A&M University, College Station, Texas 77843
³⁵Texas Tech University, Lubbock, Texas 79409
³⁶Istituto Nazionale di Fisica Nucleare, University of Trieste/Udine, Italy
³⁷University of Tsukuba, Tsukuba, Ibaraki 315, Japan
³⁸Tufts University, Medford, Massachusetts 02155
³⁹Waseda University, Tokyo 169, Japan
⁴⁰University of Wisconsin, Madison, Wisconsin 53706
⁴¹Yale University, New Haven, Connecticut 06520
- (Received 21 September 1998; published 21 January 1999)

We present a measurement of Z^0 boson and Drell-Yan production cross sections in $\bar{p}p$ collisions at $\sqrt{s} = 1.8$ TeV using a sample of 107 pb^{-1} accumulated by the Collider Detector at Fermilab. The Drell-Yan cross section is measured in the mass range of $M_{\mu\mu} > 40 \text{ GeV}/c^2$. We compare the measurements with the predictions of quantum chromodynamics in both leading order and next-to-leading order, incorporating the recent parton distribution functions. The measurements are consistent with the standard model expectations. [S0556-2821(99)01603-3]

PACS number(s): 13.60.Hb, 12.38.Qk, 13.38.Dg, 13.85.Qk

I. INTRODUCTION

In 1970, Drell and Yan developed a model for the production of massive lepton pairs in hadron-hadron collisions [1]. The Drell-Yan processes are

$$h_1 + h_2 \rightarrow l\bar{\nu}_l + X$$

$$\rightarrow l^+ l^- + X, \quad (1.1)$$

where $l = (e, \mu, \tau)$ and ν_l is the corresponding neutrino. In the standard model, the lepton pair is produced via intermediate vector bosons: $W \rightarrow l\bar{\nu}_l$ or $\gamma^*/Z \rightarrow l^+ l^-$. The Drell-Yan

process probes the structure of hadrons in a manner analogous to deep inelastic lepton-nucleon scattering (DIS). The DIS processes

$$\begin{aligned} l + N &\rightarrow l + X \\ \nu_l + N &\rightarrow \nu_l + X \\ \bar{\nu}_l + N &\rightarrow l + X \end{aligned} \quad (1.2)$$

where N is a nucleon, and the Drell-Yan processes are related. The DIS processes are the t-channel equivalents of the s-channel Drell-Yan processes.

In $\bar{p}p$ collisions at the Fermilab Tevatron, W and γ^*/Z bosons are primarily produced by quark and anti-quark annihilations

$$\begin{aligned} \bar{q}_1 + q_2' &\rightarrow W \rightarrow l \bar{\nu}_l \\ \bar{q}_1 + q_2 &\rightarrow \gamma^*/Z \rightarrow l^+ l^- \end{aligned} \quad (1.3)$$

The Drell-Yan process probes the structure of protons at the scale $Q^2 = M^2$, where Q is the 4-momentum transfer and M the boson mass. At the Tevatron, this scale can be quite large: up to $s = (1.8 \text{ TeV})^2$. From W boson production, information on parton distribution functions (PDFs) can be extracted from the decay lepton's charge asymmetry in rapidity. In leading order QCD, the W boson production cross section is directly proportional to the u-quark, $u(x)$, and d-quark, $d(x)$, momentum density functions. The variable x is the quark momentum fraction. The charge asymmetry measurement has been used to extract precise information on the slope of $d(x)/u(x)$ in the proton [2] over $0.007 < x < 0.27$. For γ^*/Z production, the leading order cross section is directly proportional to a sum of products of identical quark density functions

$$\sigma \propto \sum_q f_q q(x_1) q(x_2) \quad (1.4)$$

where the sum is over the quark (and anti-quark) density functions, and f_q is a factor that contains the quark-lepton coupling to the γ^*/Z^0 , the propagator pieces, etc. The kinematic variables (x_1, x_2) can be fully reconstructed from final state lepton pairs as e^+e^- and $\mu^+\mu^-$. Thus, by measuring the differential cross section as a function of the ee and $\mu\mu$ invariant mass and boson rapidity (y) [3], information on PDFs can also be obtained.

Previously, the Collider Detector at Fermilab (CDF) experiment has measured [4] the Drell-Yan differential cross section:

$$d^2\sigma/dMdy|_{|y|<1} \equiv \frac{1}{2} \int_{-1}^1 \frac{d^2\sigma}{dMdy} dy. \quad (1.5)$$

The measurement covers the mass range $11 < M < 150 \text{ GeV}/c^2$ and is obtained from dielectons (ee) and dimuons ($\mu\mu$) from $\approx 4 \text{ pb}^{-1}$ of $\bar{p}p$ collisions taken during the 1988–1989 collider run. The results at low mass were shown to be consistent with a $1/M^3$ dependence of

$d^2\sigma/dMdy|_{|y|<1}$ as is expected for the annihilation of point-like quarks and anti-quarks into virtual photons. At the time, the measurement favored PDFs which had the largest quark contribution in the x interval 0.006 to 0.03, in particular, the sets of PDFs which had been extracted from the most recent DIS data.

The analysis presented here is based on dimuons from the 1992–1993 and 1994–1995 collider runs. The integrated luminosity from the 1992–1993 run is $18.8 \pm 0.7 \text{ pb}^{-1}$ and the integrated luminosity from the 1994–1995 run is $88.6 \pm 7.1 \text{ pb}^{-1}$. The total Z boson cross section, the Drell-Yan differential cross section, $d^2\sigma/dMdy|_{|y|<1}$, and the shape of the y distribution for the Z mass region are measured. The total Z boson cross section is obtained from dimuons spanning the mass range, $66 < M < 116 \text{ GeV}/c^2$. The Drell-Yan differential cross section measurement covers the mass range $M_{\mu\mu} > 40 \text{ GeV}/c^2$. This corresponds to a probed region in x of 0.02 and above. The y distribution for dimuons in the $66 < M < 116 \text{ GeV}/c^2$ region is measured over $|y| < 1$. These measurements test QCD calculations and the consistency of PDFs used in those calculations.

The Drell-Yan cross section at high mass is sensitive to new physics. The high mass $\mu\mu$ data has already been used to set limits on quark-lepton compositeness [5] and new heavy neutral gauge boson production [6].

A description of the detector is given in Sec. II. The data selection is described in Sec. III. The Monte Carlo simulation used to calculate the acceptance and other quantities is described in Sec. IV. A description on muon selection efficiencies is given in Sec. V. Section VI describes the backgrounds. Section VII describes the measurement of the Z cross section. Section VIII describes the measurement of the Drell-Yan production cross section and gives the rapidity distribution in the Z region.

II. DATA ACQUISITION

A. Detector

The Collider Detector at Fermilab (CDF) is a solenoidal magnetic spectrometer surrounded by projective tower geometry calorimeters and outer muon detectors. The CDF detector is described in detail elsewhere [7]. We briefly describe the detectors that are used in this measurement. An elevation view of one quarter of the CDF detector is shown in Fig. 1.

The magnetic spectrometer consists of a 1.4 T axial magnetic field, a central tracking chamber (CTC) which is an 84 layer cylindrical drift chamber, and a vertex tracking chamber (VTX). The VTX determines the $\bar{p}p$ collision point along the beam line (z axis) and constrains the origin of track helices. This spectrometer measures the lepton charge and momentum. The momentum resolution for beam-constrained tracks is $\delta P_T/P_T^2 \approx 0.001$, where P_T is in GeV/c .

The calorimeters used in this analysis are the central electromagnetic and hadronic sampling calorimeters. They cover the pseudorapidity [3] region $|\eta| < 1.1$. The central electromagnetic calorimeter (CEM) and the central hadron calorim-

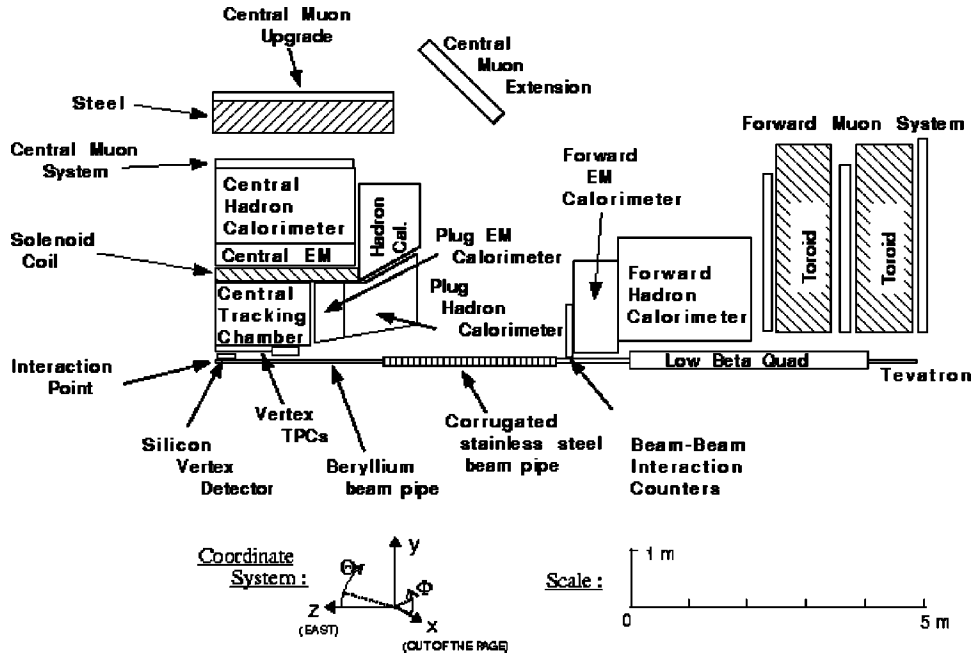


FIG. 1. One-quarter of the CDF detector. The detector is symmetric about the interaction point.

eter (CHA) have complete coverage in ϕ . The CHA provides pulse timing information from time to digital converters (CHA TDC). These TDC's measure the time elapsed with respect to the beam-beam crossing for particles that traverse the scintillators in the CHA. The calorimeters have a projective tower geometry. They are constructed as 24 "wedges" in ϕ for $\eta < 0$ and 24 "wedges" for $\eta > 0$. Each wedge consists of 10 electromagnetic towers and 8 hadronic towers. The energy resolution of the CEM is $13.5\%/\sqrt{E_T} \oplus 2\%$, and the resolution of the CHA is $50\%/\sqrt{E_T} \oplus 3\%$ (where E_T is in GeV).

Muons are reconstructed and identified using the information from the tracking devices, the electromagnetic and hadronic calorimeters, and the muon detectors. The muon detectors are drift chambers that are outside of the hadronic calorimeters in the central region. There are three muon detectors: the central muon detector (CMU [8]), the central muon upgrade detector (CMP [9]), and the central muon extension detector (CMX). The CMU is located behind five absorption lengths of material and consists of four layers of drift chambers covering 84% of the solid angle for $|\eta| \leq 0.6$. The CMP is located behind an additional three absorption lengths of material and covers 63% of the solid angle for $|\eta| \leq 0.6$. The CMP significantly reduces misidentification of hadrons as muons. About 53% of the solid angle for $|\eta| \leq 0.6$ is covered by both detectors. The CMX detector covers the pseudorapidity region, $0.6 < |\eta| < 1.0$. It has four layers of drift tubes sandwiched between scintillation counters.

B. Trigger

A three-level trigger selects the muons used in this analysis. The level 1 central inclusive muon trigger requires a muon track in the CMU with $P_T > 6$ GeV/c. Where CMP

coverage is available, $P_T > 3$ GeV/c in the CMP is also required. The P_T of a muon track is determined by the bend angle of the track measured by muon drift chambers. The level 1 trigger for the CMX detector is similar to the CMU one, and the scintillation counters on both sides of the CMX are used in the trigger.

The level 2 triggers require the tracks in the muon detectors to match tracks in the CTC found by the Central Fast Tracker (CFT) [10], a hardware track processor. These tracks must match within 5° in azimuthal angle. Tracks were required to have $P_T > 9.2$ GeV/c for 1992–1993 data and $P_T > 12$ GeV/c for 1994–1995 data. The level 2 muon trigger coverage in η – ϕ space is shown in Fig. 2. This analysis only uses level 2 triggers in the $|\eta| \leq 0.6$ region; this covers $\sim 42\%$ of the area in η – ϕ space. There are two types of level 2 triggers used in this analysis. The first trigger (CMUP) selects events in the detector regions covered by both the CMU and the CMP, and the second (CMNP) trigger selects events in the detector regions covered only by the CMU. About 90% of the data selected by the CMNP trigger in the 1994–1995 data was pre-scaled with a pre-scale factor that varied between 1 and 40. The pre-scale factor is set dynamically using an algorithm which is based on the instantaneous luminosity during data taking. The average prescale factor during the 1994–1995 run was 2.0. The CMX trigger covers the pseudorapidity range $0.6 < |\eta| < 1.0$. In this analysis, the CMX trigger is only used in the measurement of the CMUP and CMNP trigger efficiencies.

The level 3 trigger performs a full event reconstruction. At level 3, the inclusive muon trigger requires a track in a muon detector that is matched in the azimuthal plane to a CTC track which has been fully reconstructed in three dimensions. The P_T of the muon track is required to be greater than 18 GeV/c without a beam vertex constraint.

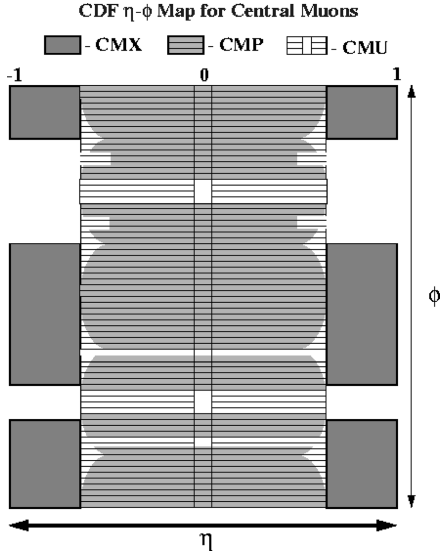


FIG. 2. The CDF level 2 trigger coverage in η - ϕ space for muons in the region of pseudo-rapidity $|\eta| \leq 1$.

III. DATA SELECTION

A. Dimuon selection

One muon is required to have $P_T \geq 20$ GeV/ c and to have passed the inclusive muon trigger. This muon is called the first muon. The other muon of the pair is called the second muon. For the Z^0 cross section analysis, the second muon is required to have $P_T \geq 20$ GeV/ c . For the measurement of the Drell-Yan production cross section, the requirement on the second muon is less restrictive: $P_T \geq 17$ GeV/ c . This increases the acceptance in the lowest mass bin. The muon momenta are reconstructed from tracks which are constrained to the $\bar{p}p$ interaction vertex using an average beam position. The reconstructed momenta are also corrected for a small misalignment of the CTC with respect to the beam axis and the magnetic field [11]. The CTC tracks of both muons are required to point back to within 5 cm of the closest event vertex location along the beam line (the $|\Delta Z_{\text{vtx}}|$ cut). The primary vertex is required to be within 60 cm of the nominal center of the detector (the $|Z_{\text{vtx}}|$ cut). The primary vertex distribution along the beam direction is approximately Gaussian with width ≈ 26 cm.

Muons originating from the Drell-Yan process are expected to be isolated from the other particles in the event. Muons from other physics processes are produced in association with jets and other particles nearby in pseudorapidity(η)-azimuthal angle(ϕ) space. To select muons which are not associated with other calorimetric activity, an isolation variable I is defined as

$$I = E_T^{\text{cone}} - E_T^{\text{cluster}}, \quad (3.1)$$

where E_T^{cone} is the sum of the EM and HAD transverse energies in all of the towers (including the muon cluster) in a radius of $R = \sqrt{(\Delta\eta)^2 + (\Delta\phi)^2} = 0.4$ centered around the muon cluster and E_T^{cluster} is the transverse energy in the muon cluster. The muon isolation I is required to be less than 4

GeV (the isolation cut) for events with a dimuon invariant mass less than 110 GeV/ c^2 . At higher dimuon invariant mass, final state QED radiation may be generated close to the muons. This lowers the efficiency at high invariant dimuon mass. Therefore, for dimuon invariant masses greater than or equal to 110 GeV/ c^2 , the isolation cut is $I < 0.1 \times P_T$. The P_T dependent isolation cut is ≈ 4.0 GeV around the Z mass, and it equals the fixed cut of 4.0 GeV used below an invariant mass of 110 GeV/ c^2 . In addition, muons from Z^0 boson production and the Drell-Yan process are required to be oppositely charged.

The muon selection cuts are given in the Table I. The first muon must have a track in the muon chambers and must pass the tight selection cuts. A match between the track in the CTC and the track segment in the CMU chambers (and CMP chambers if available) is required. The matching in the azimuthal plane ($r \times \Delta\phi$) is required to be ≤ 2.0 cm and ≤ 5.0 cm in the CMU ($|\Delta x_{\text{CMU}}|$) and the CMP ($|\Delta x_{\text{CMP}}|$) muon detectors, respectively. Wherever available, a muon segment in the CMP chamber is required. This minimizes misidentification of hadronic punchthrough as muons.

The second muon need not have a track in the muon chambers. It is required to pass the following fiducial and track quality cuts. The fiducial cut is $|\eta| \leq 1.2$. To ensure the quality of the CTC track, the muon candidate is required to have hits in at least three out of the five axial superlayers in the CTC. This track quality cut is called the N_{CTC} cut. Muons deposit a minimum ionizing signal in the calorimeters. The most probable minimum ionizing signal is ~ 0.3 GeV in the CEM and ~ 2.0 GeV in the CHA. Muons from Z^0 decays can be identified very efficiently by requiring the energy deposited in the CEM calorimeter to have $E_{\text{EM}} \leq 2$ GeV and the energy deposited in the CHA calorimeter to have $E_{\text{HAD}} \leq 6$ GeV. These requirements become less efficient as the muon energy becomes higher.

In order to maintain good efficiency for high energy muons, the minimum ionizing signal cuts are relaxed for very high muon energies. We have used the GEANT package [12] to determine the appropriate E_{EM} and E_{HAD} cut values. The CEM and the CHA muon identification energy cuts are chosen to be functions of the muon energy (E_μ) as follows:

For $E_\mu < 100$ GeV: They are $E_{\text{EM}} < 2$ GeV and $E_{\text{HAD}} < 6$ GeV.

For $E_\mu \geq 100$ GeV: Energy dependent cuts are used. They are $E_{\text{EM}} < 2 + C_1 \times (E_\mu - 100)$ GeV and $E_{\text{HAD}} < 6 + C_2 \times (E_\mu - 100)$ GeV.

The C_1 and C_2 are determined by maintaining a CEM energy cut which is 98% efficient, and a CHA energy cut which is 97% efficient: $C_1 = 0.0115$ and $C_2 = 0.0280$. These cuts are called the MIN I cuts.

B. Cosmic ray and background removal

Cosmic ray muons are the dominant source of background at high invariant mass. The suppression of the background from cosmic rays is accomplished by requiring that the two muon tracks are not consistent with a cosmic ray muon going through the detector. The first cut is based on the timing

TABLE I. List of selection requirements on both muons. The requirements on the first muon (the trigger μ) are called tight requirements. The requirements on the second muon are called loose requirements. The loose cut requirement of $P_T \geq 20$ GeV/ c is for the Z^0 cross section analysis; for the Drell-Yan cross section analysis it is $P_T \geq 17$ GeV/ c .

Type of cut	Tight cut	Loose cut
P_T	≥ 20 GeV/ c	≥ 20 GeV/ c or ≥ 17 GeV/ c
$ \Delta x_{\text{CMU}} $	< 2.0 cm	N/A
$ \Delta x_{\text{CMP}} $	< 5.0 cm	N/A
$ \Delta Z_{\text{vtx}} $	< 5.0 cm	< 5.0 cm
$ Z_{\text{vtx}} $	< 60 cm	< 60 cm
N_{CTC}	N/A	≥ 3
Isolation		
$M_{\mu\mu} < 110$ GeV/ c^2 :	$I < 4$ GeV	
$M_{\mu\mu} \geq 110$ GeV/ c^2 :	$I < 0.1 \times P_T$ GeV	
MIN I, E_{EM}		
$E_{\mu} < 100$ GeV:	$E_{\text{EM}} < 2$ GeV	
$E_{\mu} \geq 100$ GeV:	$E_{\text{EM}} < 2 + 0.0115 \times (E_{\mu} - 100)$ GeV	
MIN I, E_{HAD}		
$E_{\mu} < 100$ GeV:	$E_{\text{HAD}} < 6$ GeV	
$E_{\mu} \geq 100$ GeV:	$E_{\text{HAD}} < 6 + 0.0280 \times (E_{\mu} - 100)$ GeV	

information (CHA TDC) from the scintillators in the CHA. Dimuons originating from the $\bar{p}p$ vertex have equal flight times to the CHA. Cosmic ray muons which enter from one side of the detector and leave through the opposite side have different times of flight. The cuts on the absolute TDC values and the difference between the TDC values on the top and those on the bottom of the CDF detector are optimized to maintain a high efficiency for beam related events. For beam related events, the TDC distributions are peaked around zero. When both top and bottom TDC information exists, the CHA TDC difference $\Delta\text{TDC} \equiv \text{TDC}_{\text{top}} - \text{TDC}_{\text{bottom}}$ is required to be greater than or equal to -10 nsec, where TDC_{top} and $\text{TDC}_{\text{bottom}}$ are the timing of the top and the bottom TDC's, respectively. The individual TDC's (bottom or top) must be between -12 nsec and 16 nsec for the 1992–1993 data and -8 nsec and 20 nsec for the 1994–1995 data. The fraction of events for which CHA TDC information from both the top and bottom TDC's are available is $\approx 90\%$.

The second cut used to reject cosmic rays is the back-to-back tracking cut. The back-to-back variables are $\eta_{\text{b-b}} = \eta_1 + \eta_2$ and $\phi_{\text{b-b}} = \pi - |\phi_1 - \phi_2|$, where (η_1, ϕ_1) and (η_2, ϕ_2) are the trajectories of the two muons. The veto requirement is:

When both top and bottom CHA TDC information is available, events with both $|\eta_{\text{b-b}}| < 0.1$ and $|\phi_{\text{b-b}}| < 0.0175$ are removed.

When only the top or bottom CHA TDC information is available, events with both $|\eta_{\text{b-b}}| < 0.2$ and $|\phi_{\text{b-b}}| < 0.035$ (a larger cone) are removed.

If the two muon tracks can be fit as one continuous track, consistent with originating from a single cosmic ray muon, the event is removed.

For some cosmic rays, one side of the track is not reconstructed and the cosmic ray appears as a single track emanating from the beam line. These cosmic ray tracks usually do not intersect in z with tracks from $\bar{p}p$ interactions. To reject them, we require $|Z_{\mu_1} - Z_{\mu_2}| < 10$ cm, where Z_{μ_1} and Z_{μ_2} are the z intercepts of the tracks. All cuts used in the cosmic ray rejection are summarized in Table II.

There are two categories of backgrounds remaining after the cosmic ray rejection. The first is the charge symmetric background from typical jets. Most of these events are from hadronic punchthrough or decays in flight of pions and kaons. For this background the number of opposite charge dimuons are approximately equal to the number of same charge dimuons. Thus, this background is removed by subtracting the same-charge pairs from the opposite-charge pairs. The second category of background is from $\tau^+\tau^-$, W^+W^- , $c\bar{c}$, $b\bar{b}$, and $t\bar{t}$ production. Dimuons from this source are mostly oppositely charged. This background is measured using our $e\text{-}\mu$ data.

IV. ACCEPTANCE

A. Event simulation

A Monte Carlo program is used to determine corrections for acceptance and some of the efficiencies. The Monte Carlo program consists of an event generator based on a physics model and a subsequent detector simulation. This is used to calculate an acceptance that includes detector resolution effects. Because detector resolution effects are included in the acceptance, the physics model has been ‘‘tuned’’ so that the simulated results agree with the data.

TABLE II. Cosmic ray rejection cuts. The CHA TDC cut values in parentheses are for the 1994–1995 data.

Type of cut	TDC _{top} and TDC _{bottom} Available	Requirement
CHA TDC	$-12 \leq \text{TDC}_{\mu_1, \mu_2} \leq 16$	$-12 \leq \text{TDC}_{\mu_1(\mu_2)} \leq 16$
(nsec)	$(-8 \leq \text{TDC}_{\mu_1, \mu_2} \leq 20)$	$(-8 \leq \text{TDC}_{\mu_1(\mu_2)} \leq 20)$
ΔTDC	≥ -10 nsec	N/A
Back-to-Back	$ \eta_{b-b} \geq 0.1$ or $ \phi_{b-b} \geq 0.0175$	$ \eta_{b-b} \geq 0.2$ or $ \phi_{b-b} \geq 0.035$
$ Z_{\mu_1} - Z_{\mu_2} $		< 10 cm
Continuity	Track 1 and 2 not consistent with a single track	

The Monte Carlo program generates γ^* 's and Z 's using the lowest order diagram, $q\bar{q} \rightarrow \gamma^*/Z$ with CTEQ-3L [13] parton distribution functions. The boson masses are distributed according to a relativistic Breit-Wigner distribution. In order to mimic the kinematic effect of higher-order initial-state QCD radiation, the dileptons are generated with a P_T according to a P_T distribution of W 's as measured [14] in $\bar{p}p$ collisions at $\sqrt{s} = 1.8$ TeV. In addition, higher order QCD corrections to the mass distribution are added to the leading-order cross section by using a “ K -factor”: $K(M^2) = 1 + \frac{4}{3}(1 + \frac{4}{3}\pi^2)\alpha_s(M^2)/2\pi$ [15], where α_s is the two loop QCD coupling. For $M > 40$ GeV/ c^2 , K is 1.3–1.4. This K -factor is used as an event weight.

The generated events are passed on to the PHOTOS 2.0 [16] Monte Carlo program, which adds QED final state radiation to the γ^*/Z decay. Initial state QED radiation is not generated. PHOTOS generates QED radiative corrections for resonance decays using a leading-logarithmic, fragmentation function approximation. This has the proper soft photon behavior. The standard PHOTOS parameters are set to generate photons with energy greater than 1% of the dimuon invariant mass. This allows for double bremsstrahlung and interference between emission from the μ^+ and μ^- . Double bremsstrahlung is simulated by the double application of the leading-logarithmic algorithm. The PHOTOS differential distributions compare well with explicit $\mathcal{O}(\alpha_{em})$ matrix element calculations [16].

The QED radiative corrections from PHOTOS have been checked by using $\gamma^*(Z) \rightarrow \mu^+\mu^-$ events generated by PYTHIA [17] and subsequently processed by PHOTOS. Figure 3 shows the ratio of the cross section with QED radiative corrections ($d\sigma_f/dM$) to that without radiative corrections ($d\sigma^{DY}/dM$). The radiative corrections predicted by the PYTHIA/PHOTOS Monte Carlo simulation agree with those calculated explicitly to order $\mathcal{O}(\alpha_{em}^3)$ in a next-to-leading-logarithmic (NLL) fragmentation function formalism [18]. The cross section ratio tests QED radiative corrections because the underlying dimuon mass spectrum divides out in the ratio. The ratio is 1.8 at a dimuon mass around 60 GeV/ c^2 and 0.95 at a dimuon mass above 110 GeV/ c^2 .

The generated events with final state photons are passed on to a detector simulation. The muon curvature is smeared using the CTC tracking resolution

$$\delta p_T/p_T^2 = 0.00090 \pm 0.00009 \quad (4.1)$$

for 1992–1993 data and

$$\delta p_T/p_T^2 = 0.00112 \pm 0.00005 \quad (4.2)$$

for 1994–1995 data. The energies of the final state photons are smeared using the CEM calorimeter resolution,

$$\left(\frac{\delta E}{E}\right)^2 = \left(\frac{0.135}{\sqrt{E_T}}\right)^2 + (0.02)^2 \quad (4.3)$$

for both 1992–1993 and 1994–1995 data.

B. Acceptance calculation

The Monte Carlo program described in Sec. IV A is used to determine the kinematic and geometric acceptances for both the Z^0 cross section and the Drell-Yan differential cross section measurements. The kinematic portion of the acceptance is the efficiency of the dimuon events to pass the P_T cut. The geometric portion of the acceptance is the efficiency

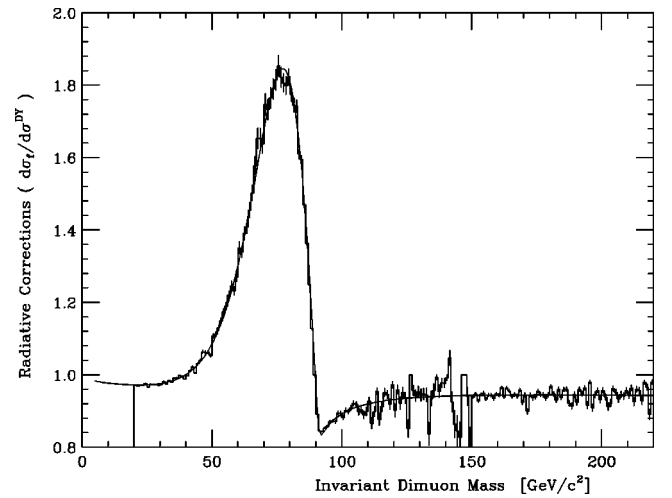


FIG. 3. The radiative correction, $d\sigma_f/dM$ to $d\sigma^{DY}/dM$ versus the $\mu^+\mu^-$ mass. The solid line is the NLL calculation, and the histogram is from PYTHIA/PHOTOS.

of the muons to traverse the fiducial and triggerable volume of the detector and to satisfy the cosmic ray back-to-back cut.

The acceptance A_Z for the Z^0 cross section measurement is calculated using

$$A_Z = \frac{N_{\mu\mu}^{\text{acc}(Z)}}{N_{\gamma^*/Z^0}^{\text{gen}}} \quad (4.4)$$

where $N_{\mu\mu}^{\text{acc}(Z)}$ is the number of accepted events in the dimuon mass range $66 < M_{\mu\mu}^{\text{sm}} < 116 \text{ GeV}/c^2$, and $N_{\gamma^*/Z^0}^{\text{gen}}$ is the number of generated γ^*/Z^0 's in the mass range $66 < M_{\mu\mu}^{\text{gen}} < 116 \text{ GeV}/c^2$. The reconstructed mass, $M_{\mu\mu}^{\text{sm}}$, is resolution smeared and includes the effect of QED radiative corrections. We extract acceptances of $(15.9 \pm 0.4)\%$ for the 1992–1993 data and $(16.8 \pm 0.4)\%$ for the 1994–1995 data. The errors are the combined Monte Carlo statistical error and systematic errors. The systematic errors are presented in Sec. VII.

The acceptance for the measurement of the Drell-Yan differential cross section, $d^2\sigma/dMdy|_{|y|<1}$, is calculated using

$$A_M = \frac{N_{\mu\mu}^{\text{acc}(M)}}{N_{|y|<1}^{\text{gen}}} \quad (4.5)$$

The acceptance A_M is for a mass bin covering the range $M(\text{low})$ to $M(\text{high})$. The $N_{\mu\mu}^{\text{acc}(M)}$ is the number of events accepted in the dimuon mass range $M(\text{low}) < M_{\mu\mu}^{\text{sm}} < M(\text{high})$. The $M_{\mu\mu}^{\text{sm}}$ is the reconstructed mass, and it is resolution smeared and includes the effect of QED radiative corrections. The $N_{|y|<1}^{\text{gen}}$ is the number of generated γ^*/Z^0 's with rapidities of $|y| < 1$ and with $M(\text{low}) < M_{\mu\mu}^{\text{gen}} < M(\text{high})$.

V. EFFICIENCIES

A. Muon identification and selection efficiencies

The muon identification and selection efficiencies used in this analysis are:

An overall combined efficiency, called “ ϵ_{tight} ,” for a muon in the CMU fiducial region to pass the tight cuts, the isolation cut, and the offline tracking.

An overall combined efficiency, called “ ϵ_{loose1} ,” for a muon in the CMU fiducial region to pass the loose cuts, isolation cut, and the offline tracking.

An overall combined efficiency, called “ ϵ_{loose2} ,” for a muon outside the CMU fiducial region to pass the loose cuts, the isolation cut, and the offline tracking. (The region outside the CMU fiducial region will be referred to as the non-CMU region.)

These efficiencies are extracted from a sample of high P_T muons. The sample is selected with criteria which are different from those used in Sec. III A. One muon must pass all the tight selection cuts. The second muon must have $P_T > 20 \text{ GeV}/c$, and its charge must be opposite to the first one. In order to obtain a more pure sample, we restrict the effi-

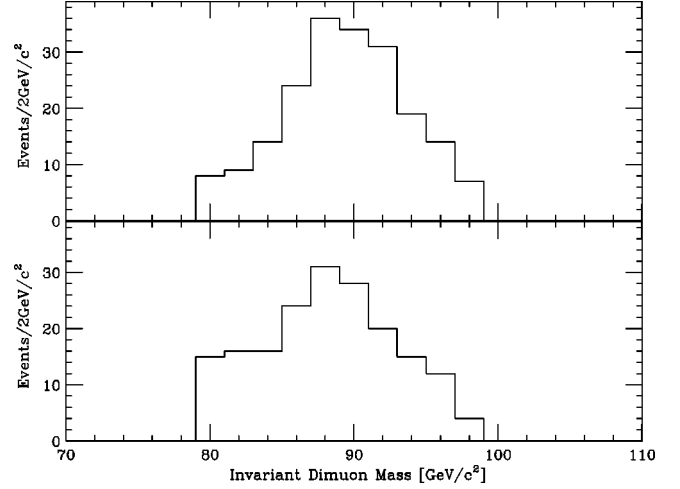


FIG. 4. Efficiency study using a sample of Z^0 events. The dimuon invariant mass distribution for the events in which the second muon fails the tight (upper plot), and the loose (lower plot) muon identification cut.

ciency sample to a narrow mass region of Z^0 decays: $80 < M_{\mu^+\mu^-} < 100 \text{ GeV}/c^2$. There are 293 events satisfying these cuts in the 1992–1993 data and 1383 events in the 1994–1995 data. The number of charge symmetric background events from typical jets is small: there are no same-sign events in the 1992–1993 data and 4 events in the 1994–1995 data. These same-sign events are subtracted in the efficiency calculation. The muon identification and selection efficiencies are measured using the second muon. Since this muon does not have any identification or selection cuts applied to it, the efficiency is the fraction that passes the cuts. Figure 4 shows the dimuon invariant mass distributions for the events which have the second muon failing the tight and the loose muon identification cut.

The muon identification and selection efficiencies are given in Table III. The $|Z_{\text{vtx}}|$ cut efficiency is not in Table III because it is applied to the event rather than to individual muons. Because of correlations between the cuts, ϵ_{tight} , ϵ_{loose1} , and ϵ_{loose2} are not products of the individual efficiencies. The offline tracking efficiency of $(99.7 \pm 0.1)\%$ is inde-

TABLE III. Efficiency of the tight cuts (ϵ_{tight}), the CMU loose cuts (ϵ_{loose1}), and the non-CMU loose cuts (ϵ_{loose2}).

Cut	1992–1993 data Efficiency (%)	1994–1995 data Efficiency (%)
MIN I	96.7 ± 0.8	96.1 ± 0.4
$ \Delta Z_{\text{vtx}} $	$100.0^{+0.0}_{-0.3}$	99.9 ± 0.1
$ \Delta x_{\text{CMU}} , \Delta x_{\text{CMP}} $	95.7 ± 1.2	94.3 ± 0.6
I	97.9 ± 0.6	98.0 ± 0.3
N_{CTC}	99.5 ± 0.4	99.5 ± 0.2
Tracking efficiency	99.7 ± 0.1	99.7 ± 0.1
ϵ_{tight}	88.1 ± 1.9	86.3 ± 1.1
ϵ_{loose1}	91.9 ± 1.5	92.1 ± 0.7
ϵ_{loose2}	93.4 ± 2.0	91.7 ± 1.1

TABLE IV. Summary of trigger efficiency calculation.

1992–1993 DATA SET				
Reference Trigger	Trigger Examined	Pass	Candidates	Efficiency
CMUP+CMX	CMNP	15	17	0.882 ± 0.078
CMNP+CMX	CMUP	29	37	0.784 ± 0.068
1994–1995 DATA SET				
Reference Trigger	Trigger Examined	Pass	Candidates	Efficiency
CMUP only ($\int Ldt \approx 10 \text{ pb}^{-1}$)	CMNP <i>not prescaled</i>	14	14	$1.000_{-0.106}^{+0.0}$
CMUP only	CMNP <i>prescaled</i>	43	92	0.467 ± 0.052
CMNP+CMX	CMUP	186	229	0.812 ± 0.026

pendent of the other cuts and it is measured separately. A description of the extraction of the track reconstruction efficiency is given in Ref. [19].

B. Muon trigger efficiency T

The efficiency of the combined level 1 and level 2 inclusive muon trigger is measured using a sample of high P_T muons. We require two muons and that both muons pass tighter criteria than in Sec. III A.

$$\begin{aligned}
 P_T &\geq 20 \text{ GeV}/c. \\
 E_{\text{EM}} &< 2 \text{ GeV} \text{ and } E_{\text{HAD}} < 6 \text{ GeV}. \\
 |Z_\mu - Z_{\text{vtx}}| &\leq 5 \text{ cm}. \\
 I &< 2 \text{ GeV}.
 \end{aligned}$$

The cosmic rays are removed as described in Sec. III B. There are three mutually exclusive level 2 inclusive muon triggers in the central region: the CMUP trigger, the CMNP trigger, and the CMX trigger. The data set used for the physics analysis requires the CMUP or the CMNP trigger. However, to study the efficiency of these triggers, we also use the CMX trigger. In order to measure the trigger efficiency of the CMUP trigger, a CMNP or a CMX trigger is required for one of the muons, while for the CMNP trigger efficiency measurement, a CMUP or a CMX trigger is required for one of the muons. We measure the efficiency of the CMUP and CMNP triggers combined with both the level 1 trigger efficiency and the CMU and CMP drift chamber hit efficiencies. To do so, we project each muon's CTC track to the muon detectors to see if it is in the triggerable region of the CMU or CMP detectors. If it is, we use the trigger data to determine if the muon fired the CMUP or CMNP trigger. The combined hit, level 1, and level 2 trigger efficiency is the fraction of the time these triggers are set. The CMNP trigger efficiency includes the prescaling on this trigger.

The ‘‘tight’’ cuts used in the offline analysis selection of muons are more stringent than the cuts used by the level 3 trigger. Therefore, the offline selection efficiency includes the efficiency of the level 3 cuts. Table IV summarizes the result of the trigger efficiency measurements.

C. Combined efficiency ϵ_Z

In order to derive a general formula for the overall combined Z^0 trigger and event selection efficiency, we divide

events into six different categories based on the trigger geometry of dimuons in an event: CMUP-CMUP, CMNP-CMNP, CMUP-CMNP, CMNP-CMUP, CMUP-only, and CMNP-only. In each pair, the first region is for the muon passing the tight cuts.

For the CMUP-CMUP, CMNP-CMNP, CMUP-CMNP, or CMNP-CMUP categories, there are three possible outcomes for the trigger.

Both muons pass the trigger with the probability $T_{\mu_1} T_{\mu_2}$.

Only one muon passes the trigger with the probability $T_{\mu_1}(1 - T_{\mu_2}) + T_{\mu_2}(1 - T_{\mu_1})$.

Both muons fail the trigger with the probability $(1 - T_{\mu_1})(1 - T_{\mu_2})$.

The T_{μ_1} and T_{μ_2} are the muon trigger efficiencies: T_{CMUP} for muons in the CMUP region and T_{CMNP} for muons in the CMNP region. Of course, the third outcome is not in the data sample. Each event can have three possible selection outcomes.

Both muons pass tight cuts with a probability $(\epsilon_{\text{tight}})^2$.

One muon passes tight cuts while the other muon passes the loose cuts but not the tight cuts with a probability $2\epsilon_{\text{tight}}(\epsilon_{\text{loose1}} - \epsilon_{\text{tight}})$.

Both muons pass the loose cuts only.

Since only the ‘‘tight-tight’’ and ‘‘tight-loose’’ combinations are selected in the analysis, the event selection efficiency is $\epsilon_{\text{tight}}(2\epsilon_{\text{loose1}} - \epsilon_{\text{tight}})$. Since each event which passes the selection criteria also has to pass the trigger, the general efficiency formula for the first four trigger geometries is given by:

$$\begin{aligned}
 \epsilon_{\mu_1\mu_2} = & [\epsilon_{\text{tight}}(2\epsilon_{\text{loose1}} - \epsilon_{\text{tight}})] [T_{\mu_1} T_{\mu_2} + T_{\mu_1}(1 - T_{\mu_2}) \\
 & + T_{\mu_2}(1 - T_{\mu_1})].
 \end{aligned} \tag{5.1}$$

The μ_1 and μ_2 denote either CMUP or CMNP.

For the CMUP-only and the CMNP-only trigger geometries, only one of the muons is in a trigger fiducial region. The selection efficiency is given by the probability $\epsilon_{\text{tight}}\epsilon_{\text{loose2}}$. The efficiency formula for these trigger geometries is given by

$$\epsilon_\mu = \epsilon_{\text{tight}}\epsilon_{\text{loose2}} \cdot T_\mu, \tag{5.2}$$

TABLE V. Summary of event fractions \times efficiencies, ϵ_{VTX} , and ϵ_{TDC} used for ϵ_Z .

	1992–93 Z sample	1994–95 Z sample
$F_{\text{UU}} \times \epsilon_{\text{UU}}$	$0.118 \times (0.803 \pm 0.036)$	$0.115 \times (0.815 \pm 0.014)$
$F_{\text{NN}} \times \epsilon_{\text{NN}}$	$0.023 \times (0.831 \pm 0.031)$	$0.038 \times (0.445 \pm 0.006)$
$F_{\text{UN}} \times \epsilon_{\text{UN}}$	$0.030 \times (0.821 \pm 0.030)$	$0.033 \times (0.769 \pm 0.017)$
$F_{\text{NU}} \times \epsilon_{\text{NU}}$	$0.031 \times (0.821 \pm 0.030)$	$0.034 \times (0.769 \pm 0.017)$
$F_{\text{U}} \times \epsilon_{\text{U}}$	$0.569 \times (0.645 \pm 0.060)$	$0.537 \times (0.643 \pm 0.011)$
$F_{\text{N}} \times \epsilon_{\text{N}}$	$0.230 \times (0.725 \pm 0.068)$	$0.244 \times (0.417 \pm 0.047)$
ϵ_{VTX}	0.955 ± 0.011	0.955 ± 0.011
ϵ_{TDC}	0.972 ± 0.010	0.975 ± 0.006
ϵ_Z	0.647 ± 0.036	0.567 ± 0.014

where T_μ is the muon trigger efficiency: T_{CMUP} for a muon in the CMUP region and T_{CMNP} for a muon in the CMNP region.

The overall combined trigger and event selection efficiency for Z^0 events is given by

$$\begin{aligned} \epsilon_Z = & (F_{\text{UU}}\epsilon_{\text{UU}} + F_{\text{UN}}\epsilon_{\text{UN}} + F_{\text{NU}}\epsilon_{\text{NU}} + F_{\text{NN}}\epsilon_{\text{NN}} \\ & + F_{\text{U}}\epsilon_{\text{U}} + F_{\text{N}}\epsilon_{\text{N}}) \times \epsilon_{\text{VTX}} \times \epsilon_{\text{TDC}}. \end{aligned} \quad (5.3)$$

The F_{UU} , F_{UN} , F_{NU} , F_{NN} , F_{N} , and F_{U} are the fractions of the CMUP-CMUP, the CMUP-CMNP, the CMNP-CMUP, the CMNP-CMNP, the CMNP-only, and CMUP-only trigger geometry events in the sample, respectively. The F_{UU} , F_{UN} , F_{NU} , F_{NN} , F_{N} , and F_{U} are called *event fractions*. These event fractions are determined using the Monte Carlo program of Sec. IV A. The ϵ_{UU} , ϵ_{UN} , ϵ_{NU} , ϵ_{NN} , ϵ_{U} , and ϵ_{N} are the corresponding overall trigger and selection efficiencies. The quantity ϵ_{VTX} is the efficiency of the $|Z_{\text{vtx}}| < 60$ cm cut [20]. The quantity ϵ_{TDC} is the efficiency of the CHA TDC timing cut used to reject cosmic rays. It is determined using the efficiency sample of Sec. V A. Cosmic rays are removed from this sample by using a very tight back-to-back veto condition: $|\eta_{\text{b-b}}| < 0.2$ and $|\phi_{\text{b-b}}| < 0.035$.

The event fractions and efficiencies are given in Table V. The slight difference in the event fractions between the two data sets reflects dead chambers during the 1992–1993 data taking. The overall combined trigger and event selection efficiency are

$$\begin{aligned} \epsilon_Z = & 0.647 \pm 0.036 \quad \text{for the 1992–1993 data} \\ \epsilon_Z = & 0.567 \pm 0.014 \quad \text{for the 1994–1995 data.} \end{aligned} \quad (5.4)$$

The lower efficiency for the 1994–1995 data is due to the prescaling of the CMNP trigger.

D. Mass dependent efficiency ϵ_M

The efficiency calculation described in the previous section is based on a sample of Z events. These efficiencies are also used to determine the efficiencies for Drell-Yan events in the other mass bins. The dimuon mass dependence of the overall efficiency originates from three sources.

The variation of the event fractions with the dimuon mass.

The final state QED radiation is larger at high mass and affects the CEM energy cut and the calorimeter isolation cut.

The muon energy dependence of the MIN I cuts.

The dimuon mass dependence of the event fractions is extracted from the Monte Carlo (MC) simulation. The maximum variation of the event fractions at other mass bins relative to the event fractions at the Z^0 mass bin are 44.9%, 86.9%, 80.3%, 22.4%, 16.7%, and 10.3% for F_{UU} , F_{UN} , F_{NU} , F_{NN} , F_{N} , and F_{U} respectively.

The effects of final state QED radiation on the minimum ionizing particle cuts and the calorimeter isolation cuts are determined using the Monte Carlo simulation. In addition to the nominal energy deposited by the muon in the CEM, photons from final state QED radiation are also projected to the CEM and their energies are added to those towers that they intersect. Next, the E_{EM} minimum ionization cut and the calorimeter isolation cuts are applied, and the individual and combined efficiencies of those cuts are calculated. The mass dependent tight and loose cut efficiencies [$\epsilon_{\text{tight}}(M)$ and $\epsilon_{\text{loose}}(M)$] are obtained by normalizing the MC efficiencies to the data at the Z^0 mass bin:

$$\begin{aligned} \epsilon_{\text{tight}}(M) &= \epsilon_{\text{tight}} \cdot \frac{\epsilon_{\text{iso-EM}}^{\text{MC}}(M)}{\epsilon_{\text{iso-EM}}^{\text{MC}}(M_Z)} \\ \epsilon_{\text{loose}}(M) &= \epsilon_{\text{loose}} \cdot \frac{\epsilon_{\text{iso-EM}}^{\text{MC}}(M)}{\epsilon_{\text{iso-EM}}^{\text{MC}}(M_Z)}, \end{aligned} \quad (5.5)$$

where $\epsilon_{\text{iso-EM}}^{\text{MC}}(M)$ is the Monte Carlo's combined isolation and E_{EM} cut efficiency over $M(\text{low}) < M_{\mu\mu} < M(\text{high})$, and $\epsilon_{\text{iso-EM}}^{\text{MC}}(M_Z)$ is the Monte Carlo's combined isolation and E_{EM} cut efficiency over the Z^0 mass bin of $80 < M_{\mu\mu} < 100$ GeV/ c^2 .

With increasing energies, muons deposit more energy in the calorimeters due to increased energy losses from e^+e^- pair production and bremsstrahlung. The MIN I cuts are designed to maintain a nearly constant efficiency for $E_\mu \geq 100$ GeV. For $E_\mu < 100$ GeV, the MIN I cuts on E_{EM} and E_{HAD} are fixed and they become more efficient as E_μ decreases. Thus, the combined MIN I cut efficiency for a muon pair is slightly dependent on the dimuon mass. We denote this by $\epsilon_{\text{MIN I}}(M)$. The same GEANT calculation [12] used to the set the E_{EM} and E_{HAD} cut values for $E_\mu \geq 100$ GeV is used to determine $\epsilon_{\text{MIN I}}(M)$. This efficiency is renormalized into the MIN I efficiency correction function for ϵ_Z :

$$f_{\text{MIN I}}(M) = \frac{\epsilon_{\text{MIN I}}(M)}{\epsilon_{\text{MIN I}}(M_Z)}, \quad (5.6)$$

where $\epsilon_{\text{MIN I}}(M)$ is the efficiency over $M(\text{low}) < M_{\mu\mu} < M(\text{high})$ and $\epsilon_{\text{MIN I}}(M_Z)$ is the efficiency over the Z^0 mass bin of $80 < M_{\mu\mu} < 100$ GeV. The efficiency correction function $f_{\text{MIN I}}(M)$ is shown as the solid curve in Fig. 5.

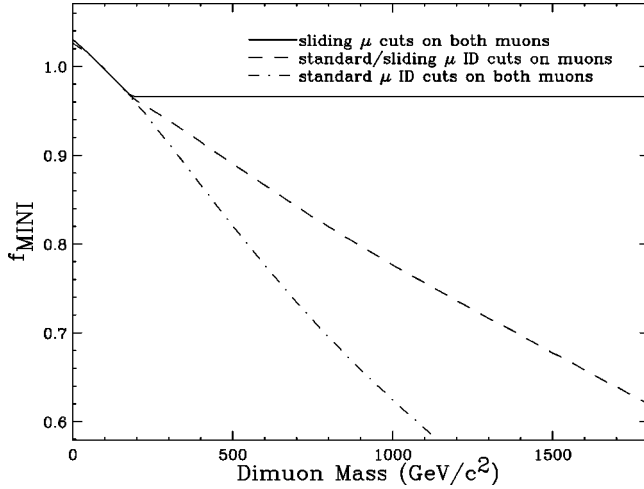


FIG. 5. The efficiency correction function for the MIN I cuts from a GEANT simulation. These functions are calculated assuming that average muon momenta are approximately factor of 1.1 larger than $M_{\mu\mu}/2$. The solid line is for the MIN I cuts ($f_{\text{MIN I}}(M)$). This is used in the Drell-Yan cross section analysis. The dashed line illustrates the case where the triggering muon passes the fixed $E_{\text{EM}} < 2$ GeV and $E_{\text{HAD}} < 6$ GeV cuts and the second, non-triggering muon passes the MIN I cuts. The dot-dash line illustrates the case where both muons pass fixed E_{EM} and E_{HAD} cuts.

The first step in calculating the overall efficiency is to convolute the mass dependent event fractions, tight cut efficiency, loose cut efficiency, trigger efficiency, etc. as is done for ϵ_Z [see Eq. (5.3)]. The next step is to factor in $f_{\text{MIN I}}(M)$. This gives the overall efficiency, ϵ_M . The values of the mass dependent efficiencies are summarized in Table VI.

TABLE VI. Summary of the selection efficiencies for the combined 1992–1993 and 1994–1995 data sets. The dip in the efficiency near 70 GeV is due to events with QED radiation (see Fig. 3) that fail the MIN I or isolation cuts.

Mass Bin GeV/ c^2	$f_{\text{MIN I}}$	ϵ_M
40–50	1.016	0.643 ± 0.030
50–60	1.012	0.619 ± 0.026
60–70	1.009	0.547 ± 0.022
70–78	1.004	0.513 ± 0.020
78–86	1.002	0.566 ± 0.022
86–90	1.000	0.626 ± 0.024
90–94	0.999	0.630 ± 0.024
94–102	0.997	0.635 ± 0.025
102–110	0.994	0.627 ± 0.025
110–120	0.991	0.619 ± 0.025
120–150	0.984	0.609 ± 0.024
150–200	0.968	0.596 ± 0.023
200–250	0.966	0.588 ± 0.024
250–300	0.966	0.586 ± 0.024
300–400	0.966	0.583 ± 0.024
400–500	0.966	0.584 ± 0.025

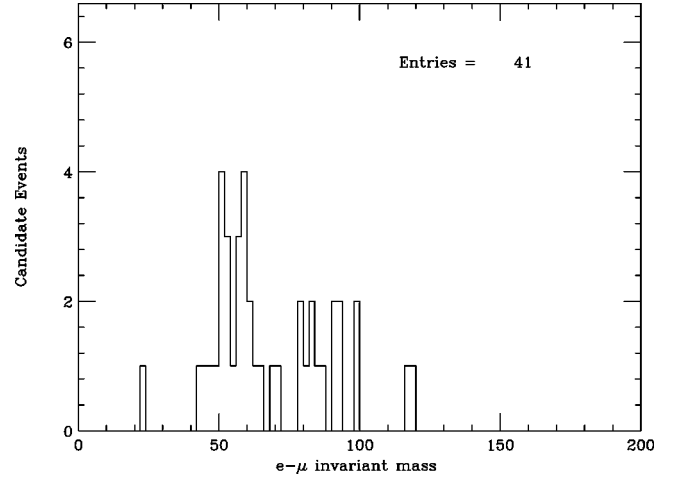


FIG. 6. e - μ invariant mass distribution for the 1992–1993 and 1994–1995 data sets combined.

VI. BACKGROUNDS

After applying the cosmic ray cuts, the cosmic ray backgrounds are estimated to be at most 0.7 events for the 1992–1993 data and 2.6 events for the 1994–1995 data. Because these upper limit estimates are very small, this background is neglected.

There is one same sign event in the data, and it occurred in the 1994–1995 running period. It is assumed that same sign events give an estimate for the backgrounds originating from the jet events.

The sum of all backgrounds originating from the $\tau^+\tau^-$, $c\bar{c}$, $b\bar{b}$, W^+W^- , and $t\bar{t}$ is small and is extracted from the e - μ sample. The e - μ selection is very similar to the e - μ selection used in the CDF top quark analysis [21]. In addition to the isolation cut for the first lepton, we apply the isolation cut for the second lepton in this background measurement.

Figure 6 shows the e - μ invariant mass distribution. This distribution is directly used in the removal of background from $\tau^+\tau^-$, $c\bar{c}$, $b\bar{b}$, W^+W^- , and $t\bar{t}$ sources. We assume half of the e - μ events is a good estimate for these backgrounds in the $\mu^+\mu^-$ channel.

VII. THE Z^0 CROSS SECTION

The measured cross section for the production of Z^0 's is obtained using

$$\sigma(Z^0) = \frac{(N_{\text{obs}} - N_{\text{bkg}}) \cdot F_Z}{\mathbf{B}(Z^0 \rightarrow \mu^+\mu^-) \cdot A_Z \cdot \epsilon_Z \cdot \int L dt}, \quad (7.1)$$

where N_{obs} is the number of observed Z^0 candidate events, N_{bkg} is the number of background events, $\int L dt$ is the integrated luminosity, $\mathbf{B}(Z^0 \rightarrow \mu^+\mu^-)$ is the Z^0 branching fraction to dimuons, A_Z is the acceptance, and ϵ_Z is the efficiency. The dimuon mass interval of this measurement is $66 < M_{\mu\mu} < 116$ GeV/ c^2 . The F_Z is a correction that accounts for continuum production and the finite mass range. The factor F_Z is

TABLE VII. Summary of the results for $\sigma(Z^0)$ using 1992–1993 and 1994–1995 data. The result for the combined 1992–1993 and 1994–1995 data is also shown. The branching fraction, $\mathbf{B}(Z^0 \rightarrow \mu^+ \mu^-) = 3.362\%$, is used.

	1992–1993 Z^0 Events	1994–1995 Z^0 Events	Combined Z^0 Events
Candidates	418	1999	2417
Backgrounds	1.3 ± 0.3	6.2 ± 1.6	7.5 ± 1.6
Signal	416.7 ± 20.5	1992.8 ± 44.7	2409.5 ± 49.2
F_Z	1.005 ± 0.002	1.005 ± 0.002	1.005 ± 0.002
A_Z	0.159 ± 0.004	0.168 ± 0.004	0.166 ± 0.004
ϵ_Z	0.647 ± 0.036	0.567 ± 0.014	0.581 ± 0.013
$\int L dt$	$18.8 \pm 0.7 \text{ pb}^{-1}$	$88.6 \pm 7.1 \text{ pb}^{-1}$	$107.4 \pm 7.1 \text{ pb}^{-1}$
$\sigma(Z^0)$	6.44 ± 0.32 (stat) ± 0.47 (syst) nb	7.06 ± 0.16 (stat) ± 0.62 (syst) nb	6.94 ± 0.14 (stat) ± 0.51 (syst) nb

$$F_Z = \frac{\int_0^\infty |Z^0|^2 dM}{\int_{66}^{116} |Z^0 + \gamma|^2 dM}, \quad (7.2)$$

where $|Z^0|^2$ is the Z^0 -only cross section and $|Z^0 + \gamma|^2$ is the γ^*/Z^0 cross section.

The results for $\sigma(Z^0)$ from the 1992–1993 and 1994–1995 dimuon data are given in Table VII. The table also includes the event counts, backgrounds, acceptances, etc. used to calculate the cross section. In the cross sections, the systematic uncertainties which are added in quadrature are from the following sources: (1) The systematic error in the measurement of the luminosity, (2) uncertainties due to choice of the different PDFs, (3) uncertainties due to the momentum measurement error, and (4) uncertainties due to the error on the measured efficiency. The uncertainties due to the error on the measured efficiency. The uncertainties due to choice of the different PDFs are estimated from the acceptance change between the default PDF, CTEQ3L, and one of the PDFs, Martin-Roberts-Stirling set A (MRS-A), CTEQ3M, and MRS-D-'. The uncertainties in the acceptance due to the error on the momentum measurement are calculated by varying the momentum resolution by ± 1 standard deviation around the central value of the measured resolution in Eq. (4.2). These uncertainties are summarized in Table VIII. Using $\mathbf{B}(Z^0 \rightarrow \mu^+ \mu^-) = 3.362\%$ [22], we find $\sigma(Z^0) = 6.44 \pm 0.57 \text{ nb}$ for the 1992–1993 data and $\sigma(Z^0) = 7.06 \pm 0.64 \text{ nb}$ for the 1994–1995 data. Independent of $\mathbf{B}(Z^0 \rightarrow \mu^+ \mu^-)$, we have $\sigma(Z^0) \cdot \mathbf{B}(Z^0 \rightarrow \mu^+ \mu^-) = 217 \pm 19 \text{ pb}$ for the 1992–1993 data and $237 \pm 22 \text{ pb}$ for the 1994–1995 data. If the common systematic errors are re-

TABLE VIII. Systematic uncertainties in the $\sigma(Z^0)$ measurements.

Sources	1992–1993 Z^0 Events	1994–1995 Z^0 Events(%)	Combined Z^0 Events
Luminosity	3.7	8.0	6.6
PDF Choice	2.6	2.5	2.2
Momentum Resolution	1.3	1.0	0.9
Efficiency	5.6	2.6	2.3

moved, the results from the 1992–1993 and 1994–1995 data differ by ~ 1.2 standard deviations. By combining both data sets, we find

$$\sigma(Z^0) = 6.94 \pm 0.53 \text{ nb}$$

$$\sigma(Z^0) \cdot \mathbf{B}(Z^0 \rightarrow \mu^+ \mu^-) = 233 \pm 18 \text{ pb}. \quad (7.3)$$

The event counts, backgrounds, acceptances, etc. of the combined data are given in Table VII.

In Fig. 7, we compare our measurement of $\sigma(Z^0) \cdot \mathbf{B}(Z^0 \rightarrow \mu^+ \mu^-)$ with our earlier results [20,23,24], the D0 measurements [25], and QCD theoretical predictions [22,26] of 222 pb with MRS-A PDFs. The dotted lines are the theoretical uncertainty of $\pm 5\%$ [27]. Table IX shows the variation in the predicted next-to-next-to-leading logarithmic (NNLO) cross section for different sets of parton distribution func-

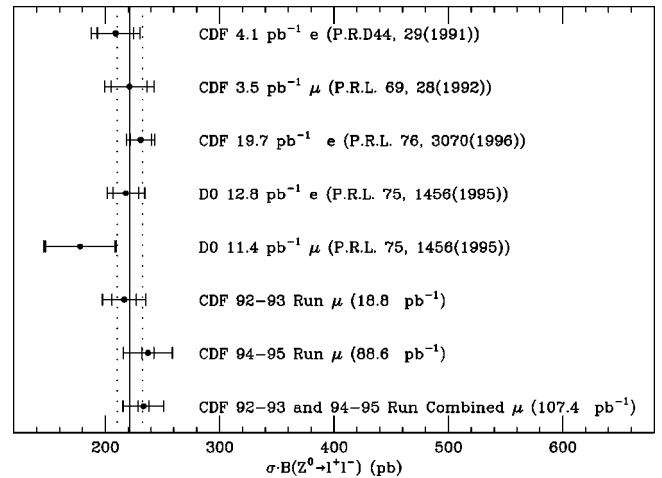


FIG. 7. Comparison of measured $\sigma(Z^0) \cdot \mathbf{B}(Z^0 \rightarrow \mu^+ \mu^-)$ to predictions (solid line) using the next-to-next-to-leading calculation with the MRS-A parton distribution functions. The dotted lines are the theoretical uncertainty of $\pm 5\%$. Also shown are earlier measurements from CDF and D0. The inner error bar is the combined statistical and systematic uncertainty and the outer error bar includes the luminosity uncertainty.

TABLE IX. The NNLO Z^0 cross sections at $\sqrt{s}=1.8$ TeV for MRS-A, CTEQ-2M, and CTEQ-3M PDFs, compared to the experimental values extracted from the dimuon 1992–1993 data set, 1994–1995 data set, and 1992–1995 combined. Also shown is the CDF 1992–1993 cross section measurement in the electron channel. The branching fraction, $\mathbf{B}(Z^0 \rightarrow e^+e^-, \mu^+\mu^-) = 3.362\%$, is used to measure $\sigma(Z^0)$.

PDF set	Channel	$\sigma(Z^0)$ (nb)
MRS-A		6.59
CTEQ-2M		6.62
CTEQ-3M		6.63
1992–93 CDF	e^+e^-	6.87 ± 0.36
1992–93 CDF	$\mu^+\mu^-$	6.44 ± 0.57
1994–95 CDF	$\mu^+\mu^-$	7.06 ± 0.64
Combined	$\mu^+\mu^-$	6.94 ± 0.53

tions [13,22,26], compared to the current CDF $\mu^+\mu^-$ measurement and the published CDF e^+e^- measurement [20].

VIII. THE DRELL-YAN PRODUCTION CROSS SECTION

The differential cross section, $d\sigma^2/dMdy_{|y|<1}$ for $\bar{p}p \rightarrow \mu^+\mu^- + X$ is obtained using

$$\frac{d^2\sigma(M_{BC})}{dMdy_{|y|<1}} = \frac{N_{\text{obs}} - N_{\text{bkg}}}{A_M \cdot \epsilon_M \cdot \int L dt \cdot \Delta M \cdot \Delta y} \cdot \frac{1}{C_{BC}}, \quad (8.1)$$

TABLE X. Summary of Drell-Yan dimuon analysis with the 1992–1993 and 1994–1995 data sets combined. The errors include both the statistical and systematic errors (including common luminosity uncertainty of 6.6% added in quadrature). N_{OS} is the number of opposite-sign events, N_{SS} is the number of same-sign events, N_{BG} is the remaining background coming from the $\tau^+\tau^-$, $c\bar{c}$, $b\bar{b}$, W^+W^- , and $t\bar{t}$, $A_M \times \epsilon_M$ is the acceptance (which includes detector resolution smearing affects) times efficiency, C_{BC} is the bin centering correction which is defined in the text, and $d^2\sigma/dMdy_{|y|<1}$ is the differential cross section. The mass bin for 400–500 GeV/ c^2 is to indicate that there is no data beyond $M=400$ GeV/ c^2 and the error for the mass bin is based on one event.

Mass Bin GeV/ c^2	N_{OS}	N_{SS}	N_{BG}	$A_M \times \epsilon_M$	C_{BC}	$d^2\sigma/dMdy_{ y <1}$ pb/(GeV/ c^2)
40–50	70	0	2.0	0.084	1.029	0.367 ± 0.057
50–60	54	1	7.5	0.161	1.020	0.129 ± 0.030
60–70	55	0	2.5	0.224	1.022	0.107 ± 0.019
70–78	63	0	0.5	0.284	1.037	0.124 ± 0.019
78–86	280	0	3.0	0.376	1.193	0.360 ± 0.037
86–90	660	0	0.5	0.241	1.349	2.36 ± 0.21
90–94	869	0	2.0	0.096	0.849	12.38 ± 1.08
94–102	449	0	1.0	0.327	1.453	0.550 ± 0.052
102–110	65	0	0.0	0.219	1.071	0.161 ± 0.025
110–120	29	0	1.0	0.181	1.040	0.069 ± 0.016
120–150	28	0	0.0	0.167	1.107	0.024 ± 0.005
150–200	9	0	0.0	0.164	1.099	0.0047 ± 0.0016
200–250	4	0	0.0	0.168	1.047	0.0021 ± 0.0011
250–300	2	0	0.0	0.169	1.032	0.00107 ± 0.00076
300–400	1	0	0.0	0.176	1.096	0.00024 ± 0.00024
400–500	0	0	0.0	0.227	1.076	0.0 ± 0.00019

where M_{BC} is the mass at the center of the mass bin, N_{obs} is the number of events in the mass bin passing the cuts, N_{bkg} is the sum of all the backgrounds, A_M is the acceptance in the mass bin, ϵ_M is the overall efficiency for the mass bin, $\int L dt$ is the total integrated luminosity, ΔM is the width of the mass bin, Δy is the rapidity interval ($=2$ in this analysis), and C_{BC} is the correction for bin centering to account for the mass centroid of the mass bin. The bin centering correction is

$$C_{BC} = \frac{\int_M^{M+\Delta M} d^2\sigma/dMdy_{|y|<1} dM/\Delta M}{d^2\sigma(M_{BC})/dMdy_{|y|<1}}, \quad (8.2)$$

where the $d^2\sigma/dMdy$ is the leading-order theoretical cross section.

A summary of the Drell-Yan dimuon analysis is given in Table X after the 1992–1993 and 1994–1995 data are combined. The systematic uncertainties from sources described in Sec. VII are summarized in Table XI. Figure 8 shows Drell-Yan cross section for the combined data. It also includes the previously published 1988–1989 CDF measurement [4]. These measurements are compared with theoretical predictions from a leading order calculation (LO+ K -factor) and a next-to-leading order calculation (NLO). In the figure, the $d^2\sigma/dMdy_{|y|<1}$ leading order cross section is calculated with the CTEQ-3L parton density functions and a K -factor (Sec. IV A) to account for higher order effects. The next-to-

TABLE XI. Systematic uncertainties in the Drell-Yan differential cross section measurement.

Mass Bin (GeV/c ²)	Sources (%)				Sum
	PDF Choice	Momentum Resolution	Efficiency		
40–50	0.7	0.1	4.6	4.6	
50–60	1.0	0.1	4.2	4.3	
60–70	1.2	0.1	4.1	4.3	
70–78	0.8	0.5	3.8	4.0	
78–86	0.5	3.0	3.9	5.0	
86–90	0.5	0.7	3.9	4.0	
90–94	0.5	2.4	3.8	4.5	
94–102	0.6	2.5	3.9	4.7	
102–110	1.4	3.9	4.0	5.8	
110–120	0.9	0.1	4.0	4.3	
120–150	0.8	0.4	4.0	4.1	
150–200	0.8	0.1	3.9	4.0	
200–250	1.2	0.2	4.1	4.3	
250–300	1.3	0.1	4.1	4.3	
300–400	1.3	0.4	4.2	4.4	
400–500	1.4	1.0	4.3	4.6	

leading logarithmic cross section is calculated using the MRS-A parton density functions. Figure 9 shows the ratio of data to theory.

Finally, we investigate the rapidity distribution of dimuons from the Z^0 cross section sample that are in the mass range, $66 < M_{\mu\mu} < 116 \text{ GeV}/c^2$. The 1992–1993 and 1994–1995 data are combined in this analysis. First, we consider the total cross section in the $|y| < 1$ region

$$\sigma = 2 \int_{66}^{116} dM \frac{d^2\sigma}{dM dy}|_{|y| < 1}. \quad (8.3)$$

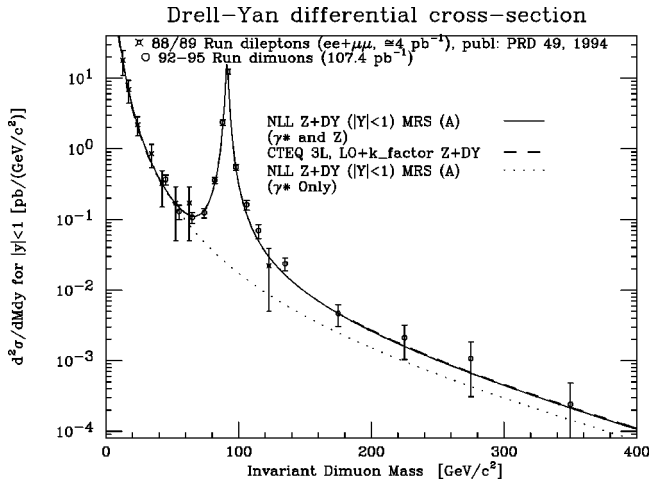


FIG. 8. Drell-Yan dimuon production cross section extracted from the combined 1992–1993 and 1994–1995 data. The solid line is the NLO QCD prediction. The dashed line is the LO QCD prediction with a K factor to account for higher order effects. The dotted line is the NLO QCD prediction without the contribution from Z^0 exchange.

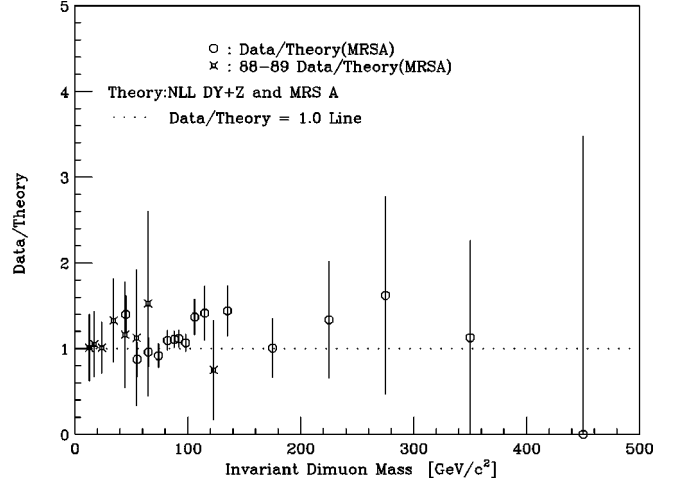


FIG. 9. The ratio of measured $d^2\sigma/dM dy|_{|y| < 1}$ (data) using the combined 1992–1993 and 1994–1995 data to the predicted $d^2\sigma/dM dy|_{|y| < 1}$ (theory).

The method used to measure the Drell-Yan cross section is used to measure σ . For the cross section, we obtain

$$\sigma = 130 \pm 10 \text{ pb}. \quad (8.4)$$

This is then used in the measurement of the cross section ratio

$$R(y) = \frac{1}{\sigma} \cdot \frac{d\sigma}{dy} \quad (8.5)$$

where $d\sigma/dy$ is the differential cross section in the boson rapidity. The $d\sigma/dy$ cross section is obtained in a manner similar to the $d^2\sigma/dM dy|_{|y| < 1}$ measurement. For the ratio, $R(y)$, the large integrated luminosity systematic error can-

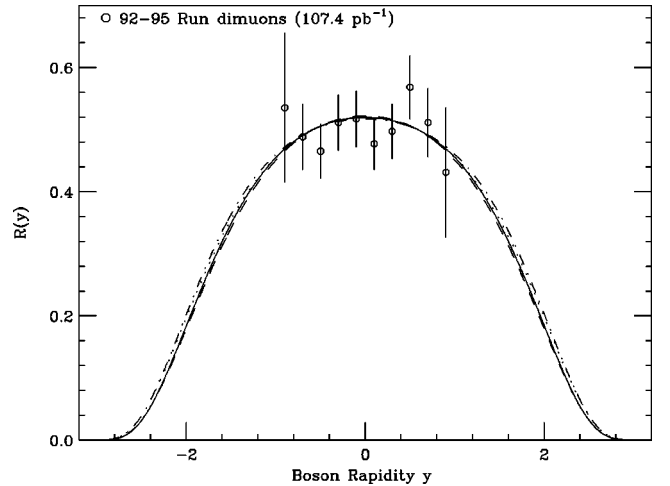


FIG. 10. The rapidity cross section ratio from the combined 1992–1993 and 1994–1995 dimuon data. The measurement is compared to leading order calculations with a K factor. The theoretical curves are calculated using the CTEQ-3L (dotted line), MRS-A (solid line), CTEQ-3M (dashed line), and MRS-D-’ (dot-dashed line) PDFs. The error includes only the statistical and the non-luminosity related systematic error.

cels out. In theoretical calculations of $R(y)$, common systematic uncertainties also cancel out. Figure 10 shows the measured cross section ratio as a function of the boson rapidity, along with theoretical predictions for various PDFs. There is good agreement with the theoretical expectations. In the $|y| < 1$ region, the ratio has a minimal sensitivity to PDFs. Thus, the measurement of the $|y| < 1$ cross section, σ , is not very sensitive to the choice of input PDFs used in the acceptance calculation.

IX. CONCLUSION

Measurements of the Z^0 and Drell-Yan differential cross sections from dimuon events are presented. The measured Z^0 cross section is consistent with a QCD calculation based on next-to-next-to-leading logarithmic calculation.

We have explicitly taken into account the final state QED radiative effects. The Drell-Yan differential cross section measurement as a function of boson mass is consistent with

our previous measurement using the dilepton events taken during 1988–89 as well as with the $LO \times K$ -factor and the next-to-leading logarithmic QCD predictions. The Drell-Yan differential cross section measurement as a function of boson rapidity in the Z^0 mass range is consistent with the $LO \times K$ -factor prediction.

ACKNOWLEDGMENTS

The vital contributions of the Fermilab staff and the technical staffs of the participating institutions are gratefully acknowledged. This work is supported by the U.S. Department of Energy, the National Science Foundation, the Natural Sciences and Engineering Research Council of Canada, the Istituto Nazionale di Fisica Nucleare of Italy, the Ministry of Education, Science and Culture of Japan, the National Science Council of the Republic of China, and the A.P. Sloan Foundation.

-
- [1] S. D. Drell and T.-M. Yan, Phys. Rev. Lett. **25**, 316 (1970).
 [2] CDF Collaboration, F. Abe *et al.*, Phys. Rev. Lett. **74**, 850 (1995); M. Dickson, Ph.D. thesis, University of Rochester, 1994; Q. Fan, Ph.D. thesis, University of Rochester, 1997.
 [3] The CDF coordinate system uses (θ, ϕ) , where θ is the polar angle relative to the proton beam, and ϕ the azimuth. The rapidity of a particle is $y = \ln[(E + P_L)/(E - P_L)]$, where E is the particle energy and P_L is its longitudinal momentum. The pseudorapidity, η , is $-\ln \tan(\theta/2)$. The transverse momentum of a particle is $P_T = P \sin \theta$. If the magnitude P is from calorimetry rather than magnetic spectrometry, the quantity is the transverse energy, E_T .
 [4] F. Abe *et al.*, Phys. Rev. D **49**, 1 (1994).
 [5] F. Abe *et al.*, Phys. Rev. Lett. **79**, 2198 (1997).
 [6] F. Abe *et al.*, Phys. Rev. Lett. **79**, 2192 (1997); M. Pillai, Ph.D. thesis, University of Rochester, 1996; E. Hayashi, Ph.D. thesis, University of Tsukuba, 1996.
 [7] F. Abe *et al.*, Nucl. Instrum. Methods Phys. Res. A **271**, 387 (1988).
 [8] G. Ascoli *et al.*, Nucl. Instrum. Methods Phys. Res. A **268**, 33 (1988).
 [9] J. Chapman *et al.* (unpublished).
 [10] G. W. Foster *et al.*, Nucl. Instrum. Methods Phys. Res. A **269**, 93 (1988).
 [11] F. Abe *et al.*, Phys. Rev. D **52**, 4784 (1995).
 [12] R. Brun *et al.*, GEANT version 3.2140, CERN Program Library Long Writeup W5013, GEANT-Detector Description and Simulation Tool.
 [13] H. L. Lai *et al.*, Phys. Rev. D **51**, 4763 (1995).
 [14] F. Abe *et al.*, Phys. Rev. Lett. **66**, 2951 (1991).
 [15] G. Altarelli, R. K. Ellis, and G. Martinelli, Nucl. Phys. **B157**, 461 (1979).
 [16] E. Barberio and Z. Was, Comput. Phys. Commun. **79**, 291 (1994); E. Barberio, B. van Eijk, and Z. Was, *ibid.* **66**, 115 (1991).
 [17] PYTHIA 5.7 is used. T. Sjöstrand, Comput. Phys. Commun. **82**, 74 (1994).
 [18] U. Baur, S. Keller, and W. K. Sakumoto, Phys. Rev. D **57**, 199 (1998).
 [19] F. Abe *et al.*, Phys. Rev. D **52**, 2624 (1995).
 [20] F. Abe *et al.*, Phys. Rev. Lett. **76**, 3070 (1996).
 [21] F. Abe *et al.*, Phys. Rev. Lett. **80**, 2779 (1998); F. Abe *et al.*, *ibid.* **74**, 2626 (1995); F. Abe *et al.*, Phys. Rev. D **50**, 2966 (1994); F. Abe *et al.*, Phys. Rev. Lett. **73**, 225 (1994).
 [22] R. Hamberg, T. Matsuura, and W. L. van Neerven, Nucl. Phys. **B359**, 343 (1991); W. L. van Neerven and E. B. Zijlstra, *ibid.* **B382**, 11 (1992).
 [23] F. Abe *et al.*, Phys. Rev. D **44**, 29 (1991).
 [24] F. Abe *et al.*, Phys. Rev. Lett. **69**, 28 (1992).
 [25] S. Abachi *et al.*, Phys. Rev. Lett. **75**, 1456 (1995).
 [26] A. D. Martin, W. J. Stirling, and R. G. Roberts, Phys. Rev. D **50**, 6734 (1994).
 [27] A. D. Martin, R. G. Roberts, W. J. Stirling, and R. S. Thorne, Eur. Phys. J. C **4**, 463 (1998).